First Principles Study of Low Miller Index RuS2 Surfaces in Hydrotreating Conditions

6 AUTHORS, INCLUDING:

Yosslen Aray
Venezuelan Institute for Scientific Research
66 PUBLICATIONS **731** CITATIONS

SEE PROFILE

Alba B Vidal
Venezuelan Institute for Scientific Research
26 PUBLICATIONS **226** CITATIONS

SEE PROFILE

Maria-Elena Grillo
40 PUBLICATIONS **282** CITATIONS

SEE PROFILE

David Santiago Coll
Venezuelan Institute for Scientific Research
33 PUBLICATIONS **253** CITATIONS

SEE PROFILE

First Principles Study of Low Miller Index RuS$_2$ Surfaces in Hydrotreating Conditions

Yosslen Aray,*,[†] Alba Beatriz Vidal,[†] Jesus Rodriguez,[†] Maria Elena Grillo,[‡] David Vega,[§] and David Santiago Coll[†]

Centro de Química, IVIC, Apartado 21827, Caracas 1020 A, Venezuela, Tyndall National Institute, Lee Maltings, Cork, Ireland, and FACYT, Universidad de Carabobo, Valencia

Density functional theory (DFT) calculations combined with surface thermodynamic arguments and the Gibbs−Curie−Wulff equilibrium morphology formalism have been employed to explore the effect of the reaction conditions, temperature (*T*), and gas-phase partial pressures (p_{H_2} and p_{H_2S}) on the stability of low Miller index ruthenium sulfide (RuS$_2$) surfaces. The calculated thermodynamic surface stabilities and the resulting equilibrium morphology models suggest that unsupported RuS$_2$ nanoparticles in HDS conditions are like to a polyhedron with six, eight, and twelve (100), (111), and (102) faces, respectively. The area of these faces covers about 40%, 37%, and 23% of the total particle, respectively. The atomic basins of the outermost individual atoms of the exposed surfaces were determined using the quantum theory of atoms in molecules methodology. Direct visualization of these basins has shown that a hole just at the middle of the outermost sulfur basins provides access to uncovered metal sites. Analysis of the electrostatic potential mapped onto a selected electron density isocontour (0.001 au) on the exposed surface reveals a very high potential reactivity of these holes toward electrodonating reagents. Consequently, the high attraction between these uncovered sites and S atoms coming from reagent polluting molecules makes these kinds of particles quite active for HDS catalysis.

1. Introduction

Transition metal sulfides (TMS) belong to a very important class of catalysts characterized by being stable under severe sulfo-reductive conditions in hydroprocessing of petroleum-based feedstock.[1,2] In hydrodesulfurization (HDS) processes, organosulfur molecules are removed from oil by reacting with hydrogen to form H$_2$S and hydrocarbons.[1−3] The catalytic process of sulfur removal involves both a C−S bond cleavage and a hydrogenation step. Studies of HDS of dibenzothiophene (DBT) over unsupported sulfides showed that the ability of a particular sulfide to catalyze the HDS reaction is related to the position of the TM in the Periodic Table. A characteristic volcano-type dependence of the activity of the metal as a function of its position in the Periodic Table, for second- (4d) and third-row (5d) transition metals was found.[4] The first-row (3d) TMS are much less active than sulfides of the second- and third-row metals, respectively. A maximum is attained for RuS$_2$, OsS$_2$, NiMoS, and Rh$_2$S$_3$, whereas Ni$_3$S$_2$ is among the less active sulfides. In HDS, the sulfide surfaces are reduced by sulfur elimination using a large excess of hydrogen at temperatures ranging from 573 to 673 K, creating coordinatively unsaturated sites (CUS) or vacancies around the metals. CUS behave as electron-withdrawing sites, whose properties may be regarded as Lewis type centers interacting with electrodonating organic substrates.[4−6] The nature of these sites is suggested to be intimately related to the metal−sulfur bond strength.[2,4,5] Fundamental studies support the view that differences in catalytic activity are related to variations in the concentration of CUS (Lewis acid sites), which in turn depend on the metal−sulfur

bond strength.[7−19] In this regard, it was found[19] that the experimental HDS[4] activities of the entire TMS series, A_{TMS}, fit on a single volcano master curve when plotted against their bulk cohesive energy per metal−sulfur bond. This correlation was corroborated[17] by means of a bond concept rigorously defined in the context of the topological theory of the electronic density, $\rho(\mathbf{r})$.

Nickel- (and cobalt) promoted molybdenum sulfide catalysts have for many years been considered to be among the most important catalysts in refinery service. However, RuS$_2$ is one of the most active TMS, making it a promising candidate to replace MoS$_2$-based catalysts to meet new and more stringent refinery requirements. Studies using X-ray absorption fine structure (EXAFS) have established that the active Mo atoms are present as small MoS$_2$-like nanostructures.[20,21] Adsorption and activity experiments[22,23] have revealed that the active sites reside at the edges of the MoS$_2$ structures. Furthermore, high-resolution scanning tunneling microscopy (STM) and density-functional theory (DFT) studies[24] have shown that the MoS$_2$ nanoclusters adopt a hexagonal shape exposing two different types of edges: Mo edges covered with S monomers and fully sulfur-saturated S. Similar studies on RuS$_2$ nanoclusters using STM[25] and theoretical calculations[26,27] on periodic surfaces have suggested that the (111) plane is responsible for the RuS$_2$ catalytic activity. The STM studies have demonstrated the formation on Au (111) substrate of hexagonal flat RuS$_2$ islands with an area of 30 nm^2. Contrary to the MoS$_2$ nanoclusters, a high density of sulfur vacancy is present on the flat (111) surface of the RuS$_2$ nanostructures. First-principles surface thermodynamics combined with Gibbs−Curie−Wulff[19,24c,28h,29−31] based morphology modeling have provide a novel way to bridge the gap between the zero-temperature (0 K) DFT results and those obtained under realistic reaction conditions. By means of this methodology a better understanding of important characteristics

* To whom correspondence should be addressed. E-mail: yaray@ivic.ve. Fax: (+58) 212 504 1350.
† IVIC.
‡ Tyndall National Institute.
§ Universidad de Carabobo.

of the active phase can be afforded. In doing so, characteristic features of the catalytic nanocrystallites, such as localization and role of the promoter, electronic properties and equilibrium morphology, can be accounted for. Particularly, effects of morphological changes of the active nanoparticles undergone upon reactions, or induced either by promoter addition or by the support, can now be addressed explicitly.

The "quantum theory of atoms in molecules" (QTAIM) of Bader et al. is very useful to obtain the chemical information from the charge density.[32–41] QTAIM is a firm, rigorous and quantum mechanically well-defined theory based on observables such as the electron density or energy density fields. QTAIM provides a quantitative link of the total electron density (regardless of how it was generated: calculated or experimental) to important physical properties of a molecule, bypassing the wave function in the analysis. QTAIM is an orbital concept free methodology. In particular, it provides a rigorous definition of chemical bond and geometrical structure for all types of molecules and solids. Additionally, QTAIM has proven to be useful in the analysis of physical properties of insulators, pure metals, and alloys.[35–39] High-quality experimental densities of minerals,[39–46] covalent,[47] metallic,[48] and molecular crystals[49–52] have been analyzed in terms of QTAIM concepts. Furthermore, QTAIM calculations on simple metals,[38,53–55] alloys, and intermetallic phases[56–60] have also been reported, as well as on molecular,[55,61–63] covalent, and ionic crystals.[39,46,47,54,64,65] QTAIM also provides a rigorous topological and quantum mechanical definition of atoms that has been identified with the atom of chemistry. These atoms have shown to recover the essential notions associated with the atomic concept: (i) the atomic properties are characteristic and additive to yield the corresponding values for the total system; (ii) they are as transferable from one system to another as are the forms of the atoms in real space (that is, as transferable as are the atomic charge distribution). In particular, atomic and group properties predicted in this manner have been shown to recover the experimentally determined contributions to the volume, energy, polarizability, and magnetic susceptibility.[32] Additionally, the most agreeable feature of QTAIM might be that it lends itself very well to visualization of the individual atoms in both complex molecular systems and condensed matter using computer graphics.

The connection between the topology of the electron density and the chemical and structural stability of isolated molecules and crystals has been well established.[17,33,35,37–39,66] Recently, the nature of the MoS$_2$[18] and NiMoS[67] catalyst edges using QTAIM was studied. Interestingly, it was found that potential active sites on the catalyst surface can be localized by direct visualization of the outermost surface atoms basin. Thus, QTAIM provides a novel an elegant way to explore the nature of the HDS active sites of the exposed surface by means of the visualization of the atomic basins of the outermost individual atoms, i.e., the volume spanned by the gradient paths ending at a given nucleus. These atoms, similarly to an atom within an isolated molecule, have considerable open parts that extend to infinity. Exposed atoms are open, or unbounded, beyond the surface. A practical atom definition[35] is to cap these atoms with an electron density, $\rho(r)$, isocontour with a small value representing the van der Waals envelope of the system. A very efficient way to visualize and quantify the strength of the active sites is to map the electrostatic potential onto this external density isocontour defining the atomic borders.[18,67]

By means a combination of the first principle surface thermodynamics, QTAIM and electrostatic potential methodologies, the nature of low Miller-index surfaces of Ni$_3$S$_2$ as HDS

catalyst was recently explored.[68] The calculated thermodynamic surface stabilities and the resulting equilibrium morphology model suggested that unsupported Ni$_3$S$_2$ nanoparticles mainly expose (111) and (11−1) type surface faces in HDS conditions. Analysis of the electrostatic potential mapped on those exposed surfaces reveals a poor potential reactivity toward electrodonating reagents (i.e., low Lewis acidity). Consequently, a very low attraction between coordinatively unsaturated active sites (Lewis sites) exposed at the catalytic particles and the S atoms coming from reagent polluting molecules makes this kind of particles rather inactive for HDS. In order to continue improving the understanding of HDS catalysts, in the present paper, we have explored the nature of low Miller-index surface of RuS$_2$ using a similar approach as that used in refs 18, 28, 67, and 68.

2. Methods

2.1. Thermodynamic Calculations. The variation of the surface coverage in a reactive atmosphere involving the presence of H$_2$ and H$_2$S in the gas/liquid phase in chemical equilibrium with the surface, as that present in industrial working conditions,[19,24c,28–31,69–71] should occur according to the reaction

$$\text{surface} + n\text{H}_2 \Leftrightarrow \text{surface-}\square_n + n\text{H}_2\text{S} \tag{1}$$

where $-\square_n$ denotes n sulfur vacancies per unit cell. The surface stability in this environment can be determined by calculating the surface Gibbs free energy, $\gamma(T,p_i)$, at temperature T and partial pressure p_i of the gas phase components. The general thermodynamic formula for $\gamma(T,p_i)$ is

$$\gamma(T,p_i) = \frac{1}{A}\left[G - \sum_i N_i\mu_i(T,p_i)\right] \tag{2}$$

here G stands for the Gibbs free energy of the solid with a surface of area A. The solid surface is modeled by a piece of material (slab) in a grand canonical ensemble at constant temperature (T) and total pressure (P). The material slab is infinite (periodic) within the surface plane with a vacuum of one nanometer separating it from its next periodically repeated image parallel to the surface. $\mu_i(T,p_i)$ is the chemical potential of the various species i present in the system, and N_i gives the number of atoms of the ith component contained in the solid slab model. For the RuS$_2$ surfaces, eq 2 can be written as

$$\gamma(T,p) = \frac{1}{2A}\left[G_{\text{RuS}_2}^{\text{slab}} - N_{\text{Ru}}\mu_{\text{Ru}}(T,p) - N_{\text{S}}\mu_{\text{S}}(T,p)\right] \tag{3}$$

where $G_{\text{RuS}_2}^{\text{slab}}$ stands for the total Gibbs free energy of a symmetric slab comprising two equivalent surfaces, μ_{Ru} and μ_{S} are the chemical potentials of a Ru atom and an S atom, respectively, and $\gamma(T,p)$ is normalized by the surface area A. Under chemical equilibrium, μ_{S} is the same in all of the phases that are in contact and contain sulfur. Hence, the following relationships between bulk RuS$_2$ and its components are satisfied:

$$\mu_{\text{Ru}} + 2\mu_{\text{S}} = \mu_{\text{RuS}_2}(\text{bulk}) \tag{4}$$

If there is enough bulk material to act as a thermodynamic reservoir the potentials are related by the Gibbs free energy of the bulk oxide

Low Miller Index RuS$_2$ Surfaces

J. Phys. Chem. C, Vol. 113, No. 45, 2009 **19547**

$$\mu_{Ru} + 2\mu_S = G_{RuS_2}(\text{bulk}) \tag{5}$$

hence, the chemical potential of Ru in the surface energy expression $\gamma(T,p)$ is equal to the corresponding chemical potential of Ru in the bulk phase

$$\mu_{Ru} = G_{RuS_2}(\text{bulk}) - 2\mu_S \tag{6}$$

Combining then eqs 3 and 6, the temperature dependence of the surface Gibbs free energy enters only through the chemical potentials of the gases in contact with the surface

$$H_2S \Leftrightarrow S_\alpha + H_2 \tag{7}$$

$$\mu_S = \mu_{H_2S} - \mu_{H_2} \tag{8}$$

$$\gamma(T,p) = \frac{1}{2A}[G_{RuS_2}^{slab} - N_{Ru}G_{RuS_2}(\text{bulk})] - \frac{1}{2}\Gamma_S\mu_S(T,p) \tag{9}$$

$$\Gamma_S = \frac{1}{A}(N_S - 2N_{Ru}) \tag{}$$

Γ_S is the surface sulfur excess with respect to a stoichiometric surface termination. Equation 9 has been generalized by Finnis[28c] for polar interfaces (e.g., grain boundary or solid surface) in multicomponent systems and has been used by numerous authors in the literature to calculate and compare the surface energy for different terminations for polar oxide and for transition metal sulphide surfaces.[19,24c,28−31]

The Gibbs free energy[28g] is associated with the Helmholtz free energy, F, via

$$G(T,p,N_{Ru},N_S) = F(T,p,N_{Ru},N_S) + pV(T,p,N_{Ru},N_S) \tag{10}$$

In general, the Helmholtz free energy can be written as

$$F(T,V,N_{Ru},N_S) = E_{DFT}^{total}(V,N_{Ru},N_S) + F^{vib}(T,V,N_{Ru},N_S) \tag{11}$$

with

$$F^{vib}(T,V,N_{Ru},N_S) = E^{vib}(T,V,N_{Ru},N_S) - TS^{vib}(T,V,N_{Ru},N_S) \tag{12}$$

comprising all contributions, which depend on vibrational modes in the system. Here E^{vib} and S^{vib} are the vibrational energy (including the zero-point energy) and entropy, respectively. The pV term is negligible[28g] ($\sim 10^{-3}$ meV/Å^2) compared to the F free energy, which is of the order of tenths of meV/Å^2. Thus, the only additional contributions to G apart from the DFT total energy are the vibrational terms

$$E^{vib} = \frac{R}{k}\frac{1}{2}\sum_i h\nu_i + \frac{R}{k}\sum_i \frac{(h\nu_i)e^{(-h\nu_i/kT)}}{[1 - e^{(-h\nu_i/kT)}]} \tag{13}$$

$$S^{vib} = R\sum_i \frac{(h\nu_i/kT)e^{(-h\nu_i/kT)}}{[1 - e^{(-h\nu_i/kT)}]} - R\sum_i \ln[1 - e^{(-h\nu_i/kT)}] \tag{14}$$

Typically, vibrational contributions to differences in the Gibbs free energies of extended systems exhibit some cancellation.[28g] If F^{vib} were completely negligible, leaving only the DFT energy as the G predominant term, the eq 9 would be rewritten as

$$\gamma(T,p) = \frac{1}{2A}[E_{RuS_2}^{slab} - N_{Ru}E_{RuS_2}(\text{bulk})] - \frac{1}{2}\Gamma_S\mu_S(T,p) \tag{15}$$

which contains exclusively terms directly obtainable from a DFT calculation. For RuO$_2$,[28g] PdO,[28e] and Cu$_2$O[28h] surfaces, rough estimation of the vibrational contribution showed that this stays below 10, 20, and 5 meV/Å^2 in the whole temperature range considered, respectively. Such a 10 meV/Å^2 contribution is certainly not a completely negligible factor; however, it was considered that this uncertainty does not affect any of the physical conclusions drawn in the studied applications. In the same way, MoS$_2$ surfaces studies[19,24c,28i,29−31] have also neglected this factor. In the present work we will include the vibrational contribution for the RuS$_2$ surfaces performing a full vibrational calculation using a standard methodology implemented in the program DMol^3.[72,73]

In practical calculations, the chemical potentials of the gas-phase mixture (H$_2$ + H$_2$S) are evaluated using the general thermodynamic formula assuming ideal gas behavior

$$\mu_S(T) = \Delta E_{el} + \Delta ZPE + \Delta H(T) - T\Delta S(T) + RT\ln\left(\frac{pH_2S}{pH_2}\right) \tag{16}$$

here $\Delta H(T)$ and $\Delta S(T)$ stand for enthalpy and entropy differences, respectively, at T for H$_2$S and H$_2$, and ΔE_{el} stands for the difference of their internal energies ($E_{el}(H_2S) - E_{el}(H_2)$), which are approximated by their zero-temperature DFT total energies. ΔZPE represents the zero-point vibrational energy term $[(H_{H_2S}(0) - E_{el}(H_2S)) - (H_{H_2}(0) - E_{el}(H_2))]$ calculated through evaluation of the Hessian matrix elements using the normal modes analysis module implemented in the program DMol^3.[72,73]

Large values of μ_S correspond to sulfur-rich conditions, whereas small values of μ_S relate to strongly reducing conditions, in which hydrogen is more abundant than H$_2$S in the gas phase. The chemical potential of sulfur, μ_S, cannot take arbitrarily large values, but it is determined by the chemical equilibrium between the surface and the gas phase. Therefore, it is necessary to determine the effect of the experimental conditions, T and gas-mixture partial pressures, upon the chemical potential of sulfur. The reduction of bulk RuS$_2$ into metallic ruthenium can be considered as the lowest limit of the sulfur chemical potential, as constrained by the chemical equilibrium

$$RuS_2 + 2H_2 \Leftrightarrow Ru + 2H_2S \tag{17}$$

This limit can be evaluated by the calculation of the Gibbs free energy of reaction according to the following equation:

19548 *J. Phys. Chem. C, Vol. 113, No. 45, 2009*

Aray et al.

$$\Delta_r G = \mu_{Ru}(\text{bulk}) - \mu_{RuS_2}(\text{bulk}) + 2\mu_S = E_{Ru}(\text{bulk}) -$$
$$E_{RuS_2}(\text{bulk}) + 2\mu_S \quad (18)$$

where the DFT total energies, $E_{Ru}(\text{bulk})$ and $E_{RuS_2}(\text{bulk})$, calculated using DMol^3 for cubic RuS$_2$ (space group Pa_3 (205)) and for bulk Ru in a face cubic center (fcc) crystal structure have been used to approximate their chemical potentials, μ_{RuS_2} and μ_{Ru}. Hence

$$\mu_S > \frac{1}{2}[E_{RuS_2}(\text{bulk}) - E_{Ru}(\text{bulk})] > -4.24 \text{ eV} \quad (19)$$

It appears that reduction should occur if μ_S is lower than -4.24 eV (i.e., $p(\text{H}_2\text{S})/p(\text{H}_2) < 10^{-5}$). Therefore, RuS$_2$ is not stable for a partial pressure ($p(\text{H}_2\text{S})/p(\text{H}_2)$) ratio lower than 10^{-5}, at which metallic ruthenium would condense at the surface.

The upper limit of sulfur chemical potential is given by the equilibrium with its crystalline α-orthorhombic phase, and it has been deduced from the Gibbs free energy change of the following reaction:

$$\Delta_r G = \mu_{S_\alpha}(\text{bulk}) - \mu_S = E_{S_\alpha}(\text{bulk}) - \mu_S \quad (20)$$

where $E_{S_\alpha}(\text{bulk})$ is the DFT total energy calculated with DMol^3 for the α-orthorhombic structure of sulfur with 128 atoms per unit cell. Thus, the upper limit is calculated to be $\mu_S < E_{S_\alpha}(\text{bulk}) < -3.08$ eV. It appears that reaction 17 becomes possible if μ_S is greater than -3.08 eV (i.e., $p(\text{H}_2\text{S})/p(\text{H}_2) > 10^4$). Thus, the variation range for μ_S (in eV) should be $-4.29 < \mu_S < -3.08$, leading to a partial pressure range of $10^{-5} < p(\text{H}_2\text{S})/p(\text{H}_2) < 10^4$ for the gas-mixture.

2.2. QTAIM Theory. The topological properties of a crystal charge distribution are summarized by its critical points (CP).[32,41] These are points where the gradient vector field, $\nabla\rho(\mathbf{r})$ vanishes, and they are classified by the $\rho(\mathbf{r})$ curvatures or three eigenvalues λ_i ($i = 1$, 2, and 3) of the Hessian matrix ($H_{ij} = \partial^2\rho(\mathbf{r})/\partial x_i\partial x_j$). They are labeled by their rank (number of nonzero eigenvalues) and signatures (excess number of positive over negative eigenvalues) and correspond to maxima (3, -3), minima (3, $+3$), and saddle points (3, $+1$) and (3, -1). Every CP has a characteristic pattern of trajectories or gradient paths of $\rho(\mathbf{r})$. The trajectories originate and end at critical points. Only the (3, -3) points are three-dimensional trajectory attractors: trajectories only terminate at this CP. The (3, -3) points occur generally at the nuclear positions so that each nucleus is a three-dimensional point attractor in the vector field $\nabla\rho(\mathbf{r})$. The region traversed by the gradient paths, which terminates at a given attractor defines the *basin* of the attractor. A (3, -1) CP, the bond critical point (*b*), is found between every pair of neighboring nuclei. It represents both, local maxima in two directions and a local minimum in the third direction. The gradient paths associated with the negative eigenvalues at the (3, -1) point terminate at this CP and define the interatomic surfaces, IAS, that partition the crystal into unique fragments (the atomic basins). In general, the interatomic boundaries of atoms within a crystal are at the interception of their interatomic surfaces.

2.3. Electrostatic Potential Methodology. Nature of active sites can be particularly explored using the electrostatic potential, $V(\mathbf{r})$, which allows the location of electron-rich sites in a molecule or crystal to be determined directly.[74-84] $V(\mathbf{r})$ at a point $\mathbf{r}$ generated by a molecule or crystal is given by

$$V(\mathbf{r}) = V_N(\mathbf{r}) + V_E(\mathbf{r}) \quad (21)$$

where the two terms $V_N(\mathbf{r})$ and $V_E(\mathbf{r})$ represent the bare nuclear and electronic contributions, respectively to the total electrostatic potential. The sign of $V(\mathbf{r})$ at a given point indicates whether nuclear (positive) or electronic (negative) effects are dominant. The electrostatic potential at $\mathbf{r}$ generated by the total charge distribution, ρ^{tot}, of a periodic system is given by

$$V(\mathbf{r}) = \sum_n \int' \rho^{\text{tot}}(\mathbf{r}' - \mathbf{R}_n)|\mathbf{r} - \mathbf{r}'|^{-1} d\mathbf{r}' \quad (22)$$

The summation extends to all direct lattice vectors. The prime on the integral sign indicates that an infinitesimal region about $\mathbf{r} = \mathbf{r}'$ is excluded from the domain of integration to avoid divergent nuclear self-interactions terms, that would otherwise arise, in the electrostatic energy per cell. ρ^{tot} might be decomposed into electronic and nuclear components

$$\rho^{\text{nuc}}(\mathbf{r}) = \sum_a q_a \delta(\mathbf{r}_a, \mathbf{r}) \quad (23)$$

where the summation extends to all the reference cell nuclei, with atomic numbers and position vectors denoted q_a and $\mathbf{r}_a$, respectively.

$$\rho^{\text{el}}(\mathbf{r}) = -\sum_{ij} \sum_{\mu\nu} P_{\mu R_i \nu R_j} \chi_\mu(\mathbf{r} - \mathbf{R}_i)\chi_\nu^*(\mathbf{r} - \mathbf{R}_i) \quad (24)$$

where P is the density matrix and $\chi_\mu(\mathbf{r} - \mathbf{R}_i)$ is the μ_{th} reference cell basis function translated by the direct lattice vector $\mathbf{R}_i$. The summations over i and j extend to all direct lattice vectors, whereas those over μ and ν include all of the basis functions of the reference cell. Substitution of eqs 24 and 23 into eq 22 gives the nuclear and electronic $V(\mathbf{r})$ contributions.

For the nearest region to the nucleus, V_N dominates and $V(\mathbf{r})$ has similar topology to the electron density[85,86] ($\rho(\mathbf{r})$), i.e., positive-valued maxima at the nuclear site and a positive-valued saddle point between every pair of bonded atoms. Nevertheless, the existence of maxima is ruled out via an established result that, barring the nuclear position, there cannot exist any strict local maxima in the $V(\mathbf{r})$ map.[77,78] For the region where V_E dominates ($V(\mathbf{r})$ is negative), the $V(\mathbf{r})$ topography can be more complex. However, it is well-known that lone pairs of electrons as well as double π bonds (C=C, C=N, etc.) are generally characterized as negative valued minima.[76,79] In summary, the nearest region to the nucleus is always positive-valued, whereas the region where the potential is negative-valued contains the minima that characterize the atom lone pairs. The minima of the negative region denote the zones to which an approaching electrophile may be attracted. On the contrary, the positive regions do not have maxima that might indicate sites for nucleophilic attack. Nevertheless, Politzer and Sjoberg have shown that by computing $V(\mathbf{r})$ on the 0.002-electron/bohr^3 contour isosurface[87] of the molecular electronic density $\rho(\mathbf{r})$ we can quantify the susceptibility of molecules to nucleophilic attack. They demonstrated that relative magnitudes of the positive electrostatic potential in various regions on this surface do reveal the sites most susceptible to nucleophilic attack. The electrostatic potential is directly related to the electronegativity in a molecular system[87] via

Low Miller Index RuS$_2$ Surfaces

J. Phys. Chem. C, Vol. 113, No. 45, 2009 **19549**

$$\chi = -\frac{\delta T_S(\rho)}{\delta \rho(r)} + V(r) - \frac{\delta E_{XC}(\rho)}{\delta \rho(r)} \qquad (25)$$

where $T_S(\rho)$ and $E_{XC}(\rho)$ are the Khon–Sham noninteracting single particle kinetic energy and the exchange-correlation energy, respectively. Since the electronegativity is constant throughout the molecular space, eq 25 suggests that it is possible to find a set of $\mathbf{r}_\chi$ values at which the equality eq 26 holds so that $\chi = V(\mathbf{r}_\chi)$.

$$-\frac{\delta T_S(\rho)}{\delta \rho(r)} = \frac{\delta E_{XC}(\rho)}{\delta \rho(r)} \qquad (26)$$

Additionally, this contour isosurface for a group of diatomic molecules and for methane encompasses at least 95% of the electronic charge and yields physically reasonable molecular dimensions.[87] The $V(\mathbf{r})$ values mapped onto this isosurface allow the host sites in which nucleophiles (most positive zone) and electrophiles (most negative zone) should bind to be identified, using a distinctive color-coding in the relevant potential energy range. Additionally, the active sites susceptibility can be quantified by determining the minimum and maximum $V(\mathbf{r})$ values at the determined host zones using a Newton–Raphson technique such as the previously reported in our study of the electronic density[18,88] and electrostatic potential topology.[83,84,89]

2.4. DFT Calculations. $\rho(\mathbf{r})$ and $V(\mathbf{r})$ were calculated by means of the Dmol^3 [72,73] program using the Kohn–Sham Hamiltonian with the gradient-corrected Perdew–Becke–Ernzerhof (PBE) exchange-correlation functional.[90] Dmol^3 calculates variational self-consistent solutions to the DFT equations, expressing numerically the atomic orbital basis functions in an accurate spherical-polar mesh. The solutions to these equations provide the molecular electron densities, which can be used to evaluate the total electrostatic potential of the system. The numerical double-ζ plus polarization basis set *DNP*[72,73] was used in all calculations. DMol^3 uses a numerical basis-set within DFT to obtain high accuracy, while keeping a relatively low computational cost compared to other ab initio methods.

3. Results and Discussion

Ruthenium disulfide bulk is a pyrite-type crystal whose lattice[91] is described by the cubic space group $Pa3$ with cube edge length a of 5.611 Å. Its structure can be described as a face-centered cube (fcc) of Ru atoms with pairs of S$_2$ molecules located in the middle of the cube edges and at the cube center.[27] Each Ru atom is bonded to six molecules in an octahedral arrangement. Each S atom has three Ru neighbors, so that a S$_2$ pair is bonded to six metal neighbors in a pseudo octahedral coordination. There is only one type of S–S and Ru–S bonds in this structure. For this crystal, three types of lowest Miller-index surfaces family can be formed: {100}, {110}, and {111} with multiplicity of six (100, −100, 010, 0−10, 001 and 00−1), twelve (110, −1−10, −110, 1−10, 101, −10−1, −101, 10−1, 011, 0−1−1, 0−11 and 01−1) and eight (111, −1−1−1, −1−11, −11−1, 1−1−1, −111, 1−11 and 11−1), respectively. STM studies[25] of ruthenium sulfide synthesized on an Au (111) surface have demonstrated the formation of a flat RuS$_2$ nanois-land with area of 30 nm^2 and a high density of sulfur vacancies located on the flat RuS$_2$ surface with a periodicity of 0.8 nm aligned along the Au lattice. The flat islands have been shown as RuS$_2$ nanocrystals with the (111) plane parallel to the Au (111) substrate. HRTEM study of RuS$_2$ nanoparticles[92] sup-ported on silica has provided atomic resolution images simula-tions. Surfaces planes such as (200) and (111) have been identified, while a recent HRTEM of RuS$_2$ supported on Al$_2$O$_3$ has suggested preferential (111), (100), (110) and (102) exposed surfaces.[93] Naked RuS$_2$ nanoparticles[94] with a narrow size distribution (2.5 ± 0.4 nm of diameter) synthesized in DMSO colloidal dispersions were characterized using atomic force microscopy, scanning electron microscopy, HRTEM, energy dispersion spectroscopy, X-ray diffraction, and absorbance and fluorescence spectroscopies. Fast Fourier transform images obtained from multiple nanoparticles image processing suggest preferential exposed planes along (111) and (210) planes.[94] In order to explore the morphology of the isolated RuS$_2$ particles at HDS conditions, we have studied the stability of the (100), (110), (111), and (102) surfaces at different sulfur coverage. The 102 surface has a multiplicity of twelve: 102, 210, 0−2−1, −10−2, 021, −2−10, 10−2, 0−21, −102, 02−1, −210, and 2−10.

To calculate the excess of energy at the surface−vacuum interface for different terminating planes, we employ symmetric slab models having two equivalent surfaces and the general theoretical approach proposed by Finnis,[28c] which has been used to calculated the energy of different surface terminations of BaTiO$_3$,[28a] Fe$_2$O$_3$,[28b] and Fe$_3$O$_4$,[28d] respectively, to name a few relevant examples. For each of the considered surface faces, the slab comprises four ruthenium layers along the surface normal. The number of sulfur atoms bonded to the Ru layers in the S−Ru−S stacking arrangement depends on the calculated surface face, as described below for each considered surface.

The (100) surface exposes the face of the bulk fcc, yielding a 2D square unit cell (see Figure 1) whose vector length corresponds to the edge of the cube ($a = b = 5.67$ Å). On each side of a Ru layer, there is an S layer. Thus, the stacking of layers can be described as a repeating stacking arrangement of S−Ru−S units (see Figure 1a). The S atoms above and below the Ru plane are bonded in inclined S$_2$ units. For maximum sulfur coverage, the outermost Ru atoms (blue spheres) are bonded to six S$_2$ pairs. Each unit cell contains two outermost Ru atoms and exposed four S atoms (red and green spheres in Figure 1) above the outermost Ru plane. Removal of the outermost S$_2$ pair (red spheres) leads to the stoichiometric surface, which exposes penta-coordinated Ru atoms.

The (110) surface, for maximum sulfur coverage, is described by a 2D rectangle ($a = 5.67$ Å, $b = 8.02$ Å, Figure 2) that contains two outermost six-coordinated Ru atoms (blue spheres) and three sulfur atoms (one red and two green spheres) above the outermost Ru layer. The stoichiometric surface is obtained by removing the outermost S layers (red spheres). Similar to the (100) surface case, this stoichiometric surface exposes 5-coordinated Ru atoms.

The (111) surface has a hexagonal unit cell ($a = 8.02$ Å, $b = 8.02$ Å) whose vectors lie along the diagonals of the cube faces (Figure 3). This unit cell contains four Ru atoms per layer and eight S atoms above the Ru plane forming four S$_2$ pairs.[26,27] Three pairs are tilted on the surface while the remaining one is oriented perpendicular to the surface with one S atom three-coordinated to the closest Ru plane and its topmost sulfur no directly bonded to ruthenium. The S atoms form four layers with slightly different heights on each side of a Ru layer. Thus, there are four S layers between two consecutive Ru layers. Similar to the bulk case, all of the Ru atoms of this surface are six-coordinated. The stoichiometric surface[26] is obtained by removing the two outermost S layers (top atoms of the S$_2$ layers). Then, all of the top S atoms correspond to broken S$_2$ pairs. On

19550 *J. Phys. Chem. C, Vol. 113, No. 45, 2009*
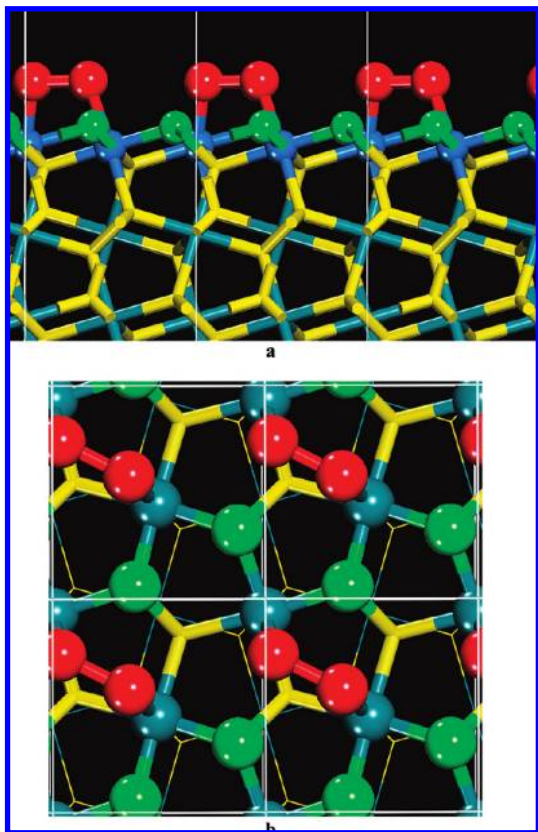
Aray et al.

Figure 1. (a) Side-view and (b) top-view of a ball and cylinders model of the RuS$_2$ (4S_100) surface. Several unit cells (white lines) are shown. Red and green spheres denote the first and second outermost sulfur atoms, respectively. Blue spheres denote the outermost ruthenium atoms. Yellow and blue cylinders denote the internal S and Ru atoms, respectively. Sequential removal of, first, the red sulfur atoms by unit cell and then the green ones produce the (3S_100), (2S_100), (1S_100), and (0S_100) surface terminations, respectively.

Figure 2. (a) Side-view and (b) top-view of a ball and cylinders model of the RuS$_2$ (2S_110) surface. Several unit cells (white lines) are shown. Red and green spheres denote the first and second outermost sulfur atoms, respectively. Blue spheres denote the outermost ruthenium atoms. Yellow and blue cylinders denote the internal S and Ru atoms, respectively. Sequential removal of, first, the red sulfur atoms by unit cell, and then, the green ones produces the (1S_110) and (0S_110) surface terminations, respectively.

the next S layer underneath, there are three S atoms in the unit cell, each one sitting on a Ru bridge site, while there is only one on the next S layer, which is located on a 3-fold Ru site. The topmost Ru plane of this surface contains six and five-coordinated atoms.

The (102) surface unit cell is described by a 2D rectangle with $a = 12.57$ Å and $b = 5.62$ Å. For maximum sulfur coverage, this cell exhibits (Figure 4) two five-coordinated Ru atoms (blue spheres) and five outermost sulfur atoms (two red and three green spheres).

For each of the above surfaces, we have studied the removal of the outermost S atoms until exposing unsaturated Ru atoms at the surface. This will be referred according to the number of exposed sulfur atoms after reduction, for example, for the (100) surface there will be (4S_100), (3S_100), (2S_100), (1S_100), and (0S_100), respectively. We have modeled these surfaces using symmetrical periodic slabs of several Ru-layers thick (at least seven) with atoms initially located at their ab initio bulk positions. Vacuum layers thicker than 15 Å were used to ensure that there were no interactions between adjacent slabs. The geometry of those models was optimized using algorithms included in the Dmol^3 program.[72,73] For the (100), (110), (111), and (102) surfaces, eight, six, eight, and four five special *k*-points generated with [4 4 1], [4 3 1], [4 4 1], and [2 4 1] meshes, respectively, along the three cell axes (and the Monkhorst−Pack scheme[72,73] were used to ensure the quality of the results. A completed structural and energetic study at 0K, using pseudo-
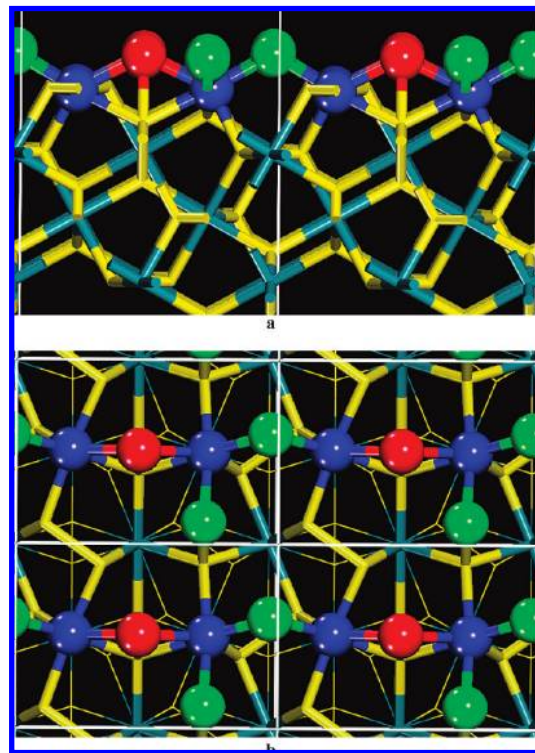
potentials, for all termination (8S_111, 7S_111, 6S_111, 5S_111, 4S_111, 3S_111, 2S_111) of the (111) surfaces has been reported.[26] We have built symmetric slabs of the asymmetric slabs used in that study... i.e., the tops and the bottoms of our slabs are similar to the tops of the models of ref 26. In general, our results agree with the findings in ref 26. At 0K, 7S_111 is the most stable termination, 4S_111 suffers an appreciable reconstruction, and a similar sulfur relaxation trend for the all terminations was observed.

In order to study the stability of these surfaces at HDS conditions (pH$_2$S/pH$_2$ = 0.05 at 650 K), their surface Gibbs free energies were calculated using eqs 9 and 16. To explore the temperature effect, the energies $\gamma(T, p(H_2S)/p(H_2))$ were determined in a T range of 400 to 850 K. In Figure 5, plots of $\gamma(T, p(H_2S)/p(H_2))$ as a function of the pH$_2$S/pH$_2$ ratios at 450, 650, and 850 K, respectively, are presented for selected surfaces. At a given pressure ratio, the lower the Gibbs free energy, the more stable the corresponding surface model. Except for the 3S_111 surface, all the surface terminations are more stable (negative slope) as the pH$_2$S/pH$_2$ ratio (and pH$_2$S) increases. These negative slopes increase with temperature. At 450 K, the 3S_100, 3S_111, and 2S_110 surfaces are the least stable over the entire range of calculated pressures. The energies of these surfaces are above the corresponding energy for the 4S_111 surface. The 7S_111 surface is the most stable one over almost the whole range of pressures (pH$_2$S/pH$_2$ > 0.001). The 2S_100, 6S_111, 5S_102, and 5S_111 surfaces are the most stable for highly reducing conditions (pH$_2$S/pH$_2$ < 0.001 and very high H$_2$ pressure) leading to the decreasing surface stability trend 2S_100 > 6S_111 ≅ 5S_102 ≅ 7S_111 > 5S_111. For pH$_2$S/

Low Miller Index RuS$_2$ Surfaces

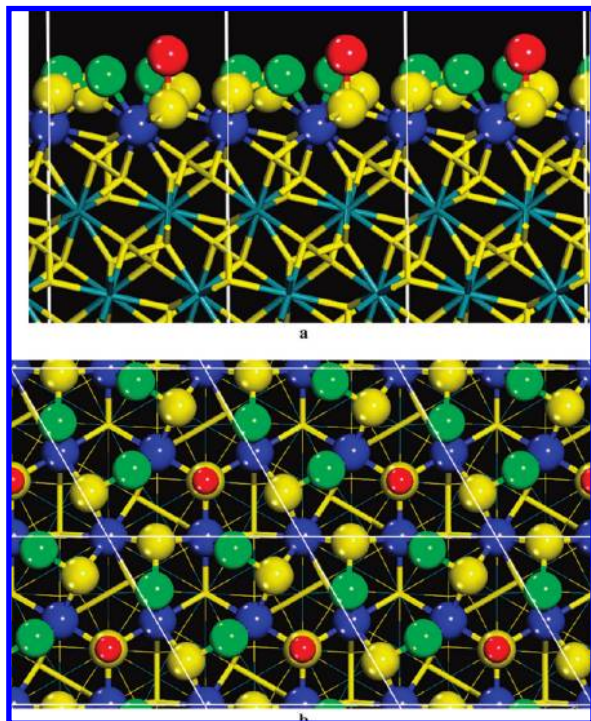*J. Phys. Chem. C, Vol. 113, No. 45, 2009* **19551**

Figure 3. (a) Side-view and (b) top-view of a ball and cylinders model of the RuS$_2$ (8S_111) surface. Several unit cells (white lines) are shown. Red, green and yellow spheres denote the first, second and third outermost sulfur atoms, respectively. Blue spheres denote the outermost ruthenium atoms. Yellow and blue cylinders denote the internal S and Ru atoms, respectively. Sequential removal of, first, the red sulfur atom by unit cell, and then, the green ones produces the (7S_111), (6S_111), (5S_111), (4S_111), (3S_111), (2S_111), (1S_111), and (0S_111) surface terminations, respectively.
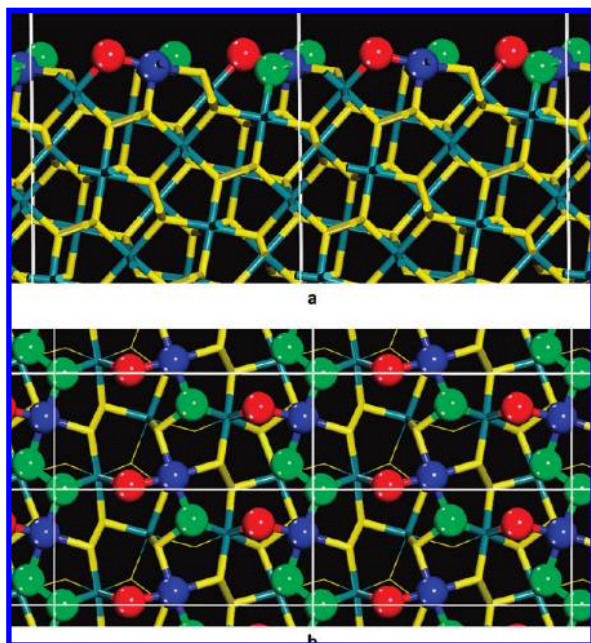

Figure 4. (a) Side-view and (b) top-view of a ball and cylinders model of the RuS$_2$ (5S_102) surface. Several unit cells (white lines) are shown. Red and green spheres denote the first and second outermost sulfur atoms, respectively. Blue spheres denote the outermost ruthenium atoms. Yellow and blue cylinders denote the internal S and Ru atoms, respectively. Sequential removal of, first, the red sulfur atom by unit cell and then the green ones produces the (4S_102), (3S_102), (2S_102), (1S_102), and (0S_102) surface teminations, respectively.
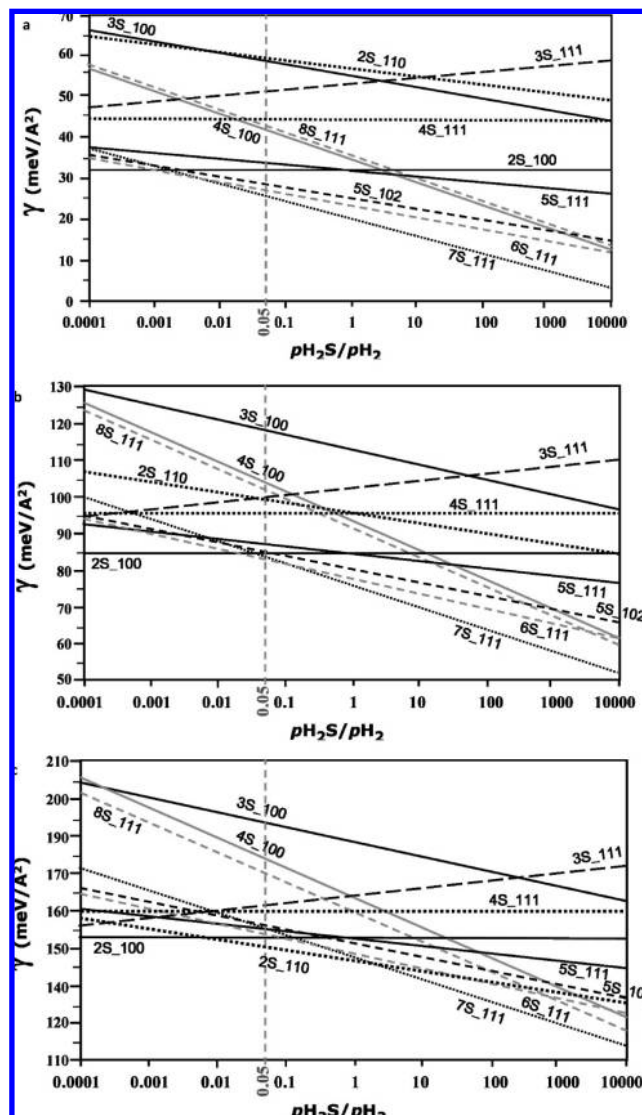

Figure 5. Variation of the surface Gibbs free energy, γ(T, pH$_2$S/pH$_2$), as a function of the pH$_2$S/pH$_2$ ratio at 450 (a), 650 (b), and 850 K (c), respectively, for the studied RuS$_2$ surfaces. Each line is labeled by the corresponding sulfur-coverage. In the plot, a pressure range of 10^{-4} <pH$_2$S/pH$_2$ <10^4 is used, corresponding to the stability of the RuS$_2$ phase. A vertical large dotted line at pH$_2$S/pH$_2$ = 0.05 shows the typical ratio at HDS conditions.

pH$_2$ > 9.0, the 4S_100 termination was the most stable S coverage for the 100 surface. The relative surfaces stability trend for these strong sulfiding conditions (pH$_2$S/pH$_2$ > 9.0 and high H$_2$S pressure) is 7S_111 > 6S_111 > 5S_102 > 4S_100 $\cong$ 8S_111 > 5S_111.

At 650 K, the 3S_100 and 3S_111 surfaces are still the least stable surfaces over almost the whole range of studied pressures, lying now in energy above the 4S_111 one. The 2S_110, 4S_100, and 8S_111 surfaces are more stable than the 4S_111 one for pH$_2$S/pH$_2$ > 1.0. The 2S_100 and 7S_111 terminations are the most stable surfaces for pH$_2$S/pH$_2$ < 0.03 and pH$_2$S/pH$_2$ > 0.1, respectively, leaving a small range (0.03< pH$_2$S/pH$_2$ < 0.1) of pressure ratio where the 6S_111 is the most stable one. The decreasing stability trend of the energy surfaces for strong reducing conditions (pH$_2$S/pH$_2$ < 0.001) is 2S_100 > 5S_111 $\cong$ 6S_111 $\cong$ 5S_102 > 4S_111 $\cong$ 3S_111, whereas for strong sulfiding conditions (pH$_2$S/pH$_2$ > 1000.0), it is 7S_111 > 6S_111 $\cong$ 8S_111 $\cong$ 4S_100 $\cong$ 5S_102 > 5S_111.

At 850 K, the 3S_100 surface remains the least stable one over almost the entire range of studied pressures. Terminations 8S_111, 4S_100, and 3S_111 are between the least stable surfaces depending on the pH_2S/pH_2 ratio. For reducing conditions ($pH_2S/pH_2 < 0.01$) these surfaces are between the least stable ones. However, for $pH_2S/pH_2 > 3.0$, the 8S_111 and 4S_100 surfaces are more stable than the 4S_111 termination. The 3S_111 surface is among the most stable one for strong reducing conditions ($pH_2S/pH_2 < 0.001$). The 2S_100 and 7S_111 surfaces are the most stable surfaces for $pH_2S/pH_2 < 0.01$ and $pH_2S/pH_2 > 4.0$, respectively. The 2S_110 surface is also particularly stable for all of the pressure ranges at 850 K, and it is just the most stable for the range of $0.01 < pH_2S/pH_2 < 4.0$. The decreasing surfaces stability trend for strong reducing conditions ($pH_2S/pH_2 < 0.001$ and high H_2 pressure) is 2S_100 > 2S_110 ≅ 3S_111 > 5S_111 ≅ 6S_111 ≅ 5S_102, whereas for strong sulfiding conditions, it is 7S_111 > 8S_111 > 6S_111 > 4S_100 ≅ 2S_110. In summary, up to 750 K, the 2S_100 and 7S_111 terminations correspond to the most stable sulfur coverage for reducing and sulfiding conditions, respectively. High temperature ($T > 750$ K) favors the stability of the 2S_110 surface at a pH_2S/pH_2 ratio close to 0.1. A low sulfur coverage such as than in the 3S_111 termination is favored for strong reducing conditions and high temperature.

The surface energy (γ) trend at each $p(H_2S)/p(H_2)$ value of Figure 5 determines the morphology (kind and area of the exposed surfaces) of the catalyst particles. The calculation of the above surface energies makes it possible to deduce the Gibbs−Curie−Wulff (GCW)[19,95] equilibrium morphology of the RuS$_2$ nanocrystallites. This law connects surface energies and particle morphology. The GCW law states that the distance of a surface plane from the center-of-mass of the particle, d_{hkl}, is proportional to the surface energy, γ_{hkl}, of that plane

$$\frac{\gamma_{1(hkl)}}{d_{1(hkl)}} = \frac{\gamma_{2(hkl)}}{d_{2(hkl)}} = \ldots \frac{\gamma_{i(hkl)}}{d_{i(hkl)}} = \text{const} \qquad (27)$$

For a crystal in equilibrium, the ratio of the energies of two orientations (γ_1 and γ_2) is equal to the ratio of the perpendicular distances from the center of the crystal to the facet (d_1 and d_2): $d_1/d_2 = \gamma_1/\gamma_2$. Thus, the lower the surface energy of the facet, the closer the facet is to the center of the crystal and the greater the surface area of the facet. This is the basis of the Wulff construction, which specifies the relationship between the surface energy of a crystal and its equilibrium shape. To apply the Wulff construction, we begin by imagining that a normal vector represents each distinct crystallographic orientation and the magnitude of each normal vector is equal to the surface energy of the orientation that it represents. Further, we assume that the vectors share a common origin. If a perpendicular plane is situated at the end of each vector, then the inner envelope of the planes defines the equilibrium crystal shape. This method has been successfully used to describe the shape of a variety of nanoscale particles.[19,24c,28h,29,30,93,96] In the present paper, we have used the KrystalShaper[97] software to determine the equilibrium shape of the RuS$_2$ particles. Applying the values of Figure 5, we have deduced the equilibrium morphologies as a function of the working conditions. The obtained shapes for the pH_2S/pH_2 zones defined in Figure 5 are shown in Figure 6. Profiles of γ as a function of pH_2S/pH_2 for the most stable surfaces, and therefore the relevant surfaces for the particles morphologies, are shown at the top of Figure 6. The sulfur coverage and the corresponding relative stability trend are shown in the middle

block panels. Blocks from white to dark gray represent pH_2S/pH_2 ranges of maximum and minimum surface stability, respectively. Hence, white blocks correspond to the pH_2S/pH_2 regime leading to the S coverage of minimum surface energy (i.e., most stable). Dotted lines parallel to the γ axe denote the transition pH_2S/pH_2 values corresponding to a change in the surface stoichiometry. For example, at 450 K, the (100) surface S coverage changes from 2S_100 to 4S_100 just at $pH_2S/pH_2 = 10$. Thus, at 450 K, the γ trend is 2S_100 (white) > 6S_111 (light gray) > 5S_102 (dark gray) for $0.0001 < pH_2S/pH_2 < 0.009$. This trend has very significant consequences for the particles shape and the nature of the active sites of the RuS$_2$ particles according to the GCW equilibrium morphology principle.

In the $0.0001 < pH_2S/pH_2 < 0.009$ range, the particle morphology will be given by a polyhedron exposing six (100), eight (111), and twelve (102) faces, respectively, as shown in the bottom left of Figure 6a. Note that the areas of the faces are proportional to the surface energy (γ). The particle shown at the left of Figure 6a corresponds to $pH_2S/pH_2 = 0.0001$. From this pressure ratio onward, the area of the (100) face starts to decrease, accompanied by a simultaneous increase in the area of the other two faces just up to a ratio of 0.001, where the (111) face is the most stable and its corresponding area the largest. The particle in the middle of Figure 6a corresponds to $pH_2S/pH_2 = 0.05$, exposing a very small (100) surface area. A little beyond that point, the 7S_111 surface starts to grow, the (100) disappears, and the area of the 5S_102 begins to decrease until very strong sulfiding conditions, where the particles become square bipyramidal (see bottom right in Figure 5a) with 100% of the eight faces corresponding to the 7S_111 surface.

Our results (see Figure 6, panels a and b) reveal that, at thermodynamic equilibrium, the RuS$_2$ particles should exhibit only the (100), (111), and (102) facets, independently of the pressure for temperatures lower than 750 K. Nonetheless, appreciable changes in the proportions and shapes of the exposed surface areas are induced by temperature and pressure effects. In general, strong reduction conditions ($pH_2S/pH_2 < 0.01$) and high temperature favors the (100) surface, while strong sulfiding conditions ($pH_2S/pH_2 > 9.0$) and low temperatures favors the (111) one. For strong sulfiding conditions, the area of the (111) face is at least 78% (at 650 K) of that corresponding to the total particle area. For strong reduction condition, the (100) surface area increases from 40% (at 450 K) to 60% (at 650 K) of the total particle area. For a typical HDS condition ($pH_2S/pH_2 = 0.05$ and $T = 650$ K), the (100), (111), and (102) surfaces correspond to about 40%, 37%, and 23% of the total particle area, respectively. At 650 K, the (100) surface shape changes from hexagons (for strong reduction conditions) to squares (for strong sulfiding conditions), while the (111) surfaces always look like deformed hexagons.

Figure 6c shows the morphology of the RuS$_2$ particles at 850 K. The appearance of the 2S_110 surface produces drastic changes in the morphology and nature of the exposed faces of the RuS$_2$ particles, namely, a polyhedron exposing six (100), eight (111), twelve (102), and twelve (110) surface cuts, respectively. In general, the 5S_102 surface only occupies less than 8% of the total area. For pH_2S/pH_2 ratios lower than 0.01, the particles mainly exhibit 2S_100, 5S_111, and 2S_110 faces each one occupying a third of the area. In the range of $0.01 < pH_2S/pH_2 < 4.0$, about 50% of the total particle area corresponds to a 2S_110 surface termination. At $pH_2S/pH_2 = 0.05$, about 40% of the total surface area is half 2S_100 and half 6S_111 terminated, respectively. For stronger sulfiding conditions ($pH_2S/$

Low Miller Index RuS₂ Surfaces

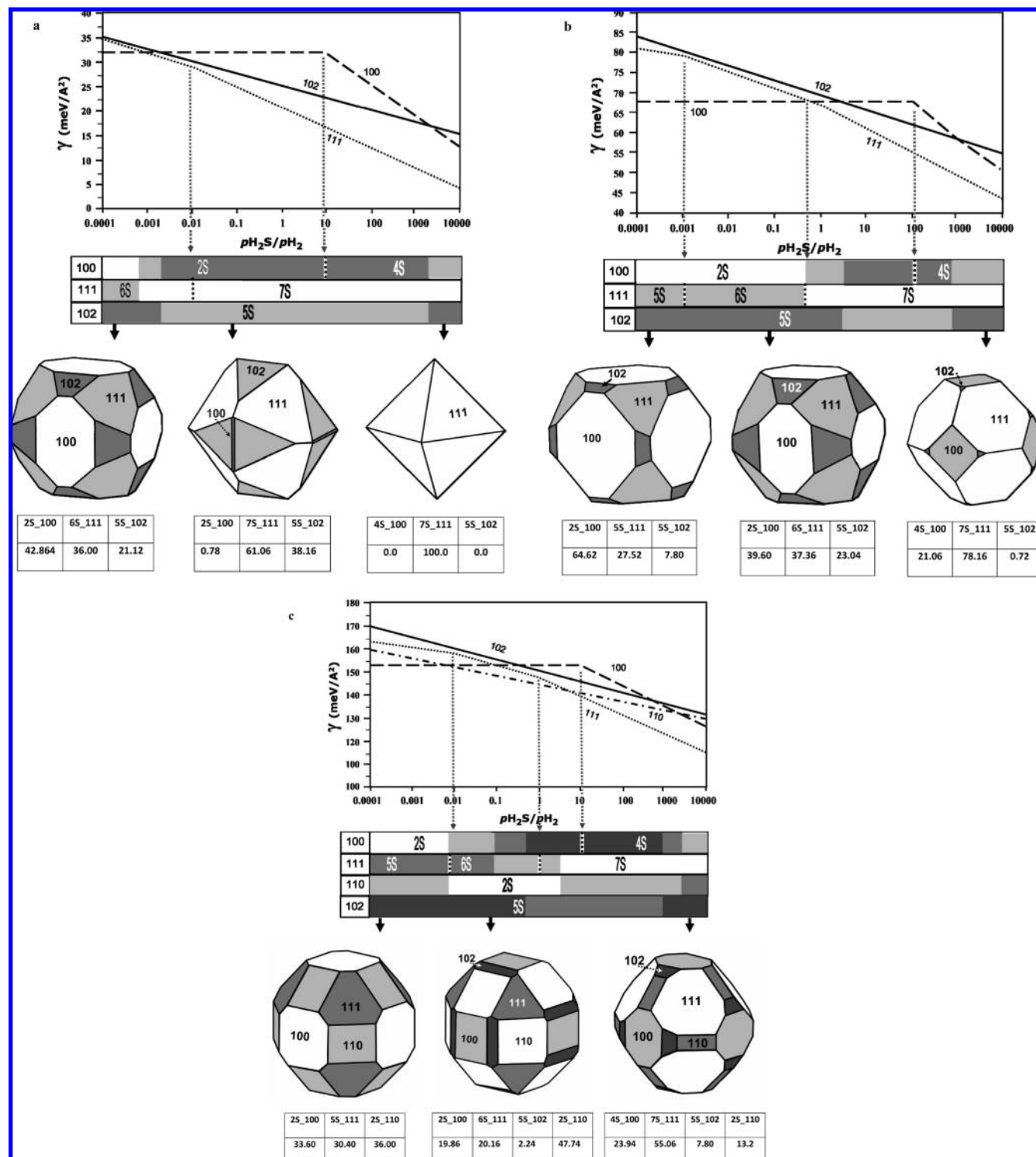*J. Phys. Chem. C, Vol. 113, No. 45, 2009* **19553**

Figure 6. RuS₂ particle morphologies calculated under different working conditions: (a) 450, (b) 650, and (c) 850 K. Surface energy diagrams as a function of the pH₂S/pH₂ ratio for the most stable RuS₂ surfaces are shown at the top the pictures. Vertical dotted lines show the transition pH₂S/pH₂ values corresponding to changes in the lowest energy surface sulfur (S) coverage. The S coverage and the corresponding relative stability trend are reported in the middle block panels. The surface energy increases from white to dark gray for a given pH₂S/pH₂ range. Hence, white and dark gray colors denote the pH₂S/pH₂ zones where the S coverage is the most and least stable, respectively The RuS₂ particle morphologies and calculated areas (Å²) for pH₂S/pH₂ = 0.0001 (left), 0.0500 (middle), and 10.0000 (right), respectively, are reported at the bottom of the panels.

pH₂ > 10.0), more than 50% of the total area is 7S_111 terminated, whereas around 20, 13, and 8% of the total particle area correspond to the 4S_100, 2S_110, and 5S_102 surfaces, respectively.

In summary, pressure and temperature affect the morphology and nature of the exposed faces. In general, strong sulfiding conditions favor the presence of surfaces with high sulfur

coverage like the 7S_111 and 4S_100 surface terminations, whereas strong reduction conditions favor surface terminations like to 5S_111 and 2S_100 with a lower S coverage. For typical HDS conditions, pH₂S/pH₂ = 0.05 and T = 650 K, the surfaces 6S_111, 2S_100, and 5S_102 are the most stable surface terminations and make an appreciable contribution to the particle total area. HR-TEM micrographs and fast Fourier transform
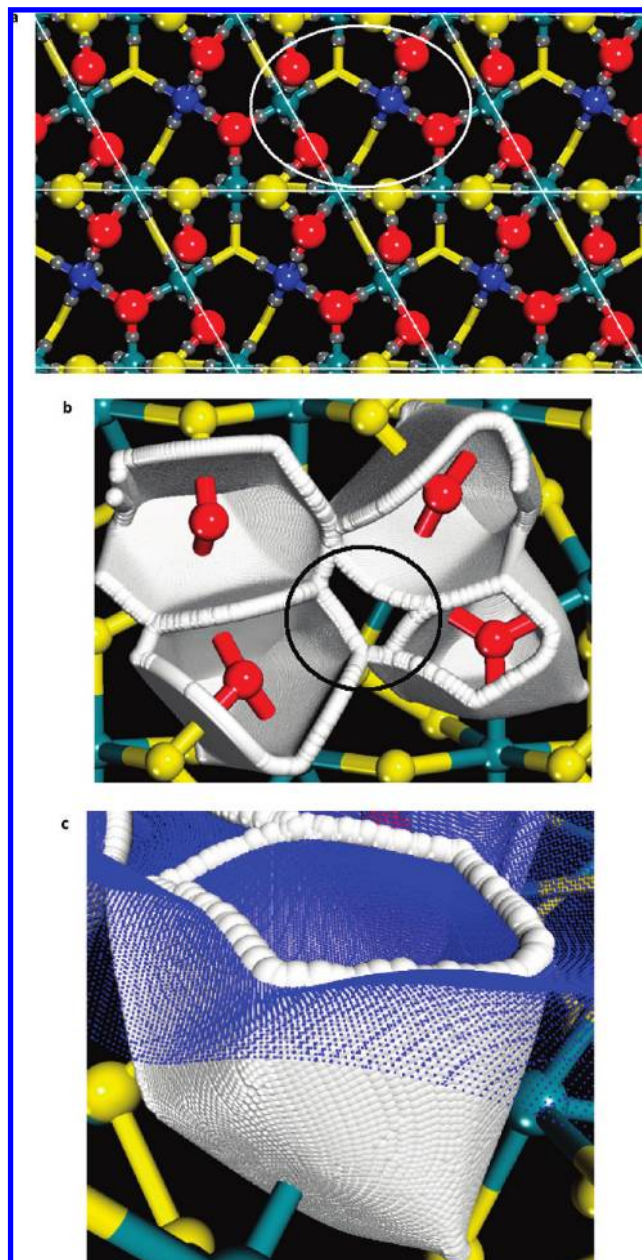
19554 *J. Phys. Chem. C, Vol. 113, No. 45, 2009*

Aray et al.

Figure 7. (a) Top-view of a ball and cylinders model of the optimized geometry of the 6S_111 surface. Several unit cells (white lines) are shown. Dark blue spheres denote the outermost 5-coordinated Ru atoms. Red spheres denote the outermost sulfur atoms closest to each outermost 5-coordinated Ru atom. Yellow and blue cylinders denote the internal S and Ru atoms, respectively. (b) Top-view of the atomic basins (white walls) of four outermost S atoms (red spheres) closest to one outermost Ru atom. A black circle highlights the hole giving access to the Ru atom. (c) Side-view of one outermost S atom basin. The $\rho(\mathbf{r}) = 0.001$ au blue iso-surface defines the outer limit that covers the atom. A white circle shown in (a) highlights the atoms involved in the isosurface marked in (b).

images of RuS2 nanocrystallites at room temperature[94] revealed preferential exposed planes of the {111} and {102} family faces while the (100) surfaces were not detected. In agreement with this finding, our results suggest (see Figure 6, panels a and b) that at temperature below 400 K and $0.1 < p\text{H}_2\text{S}/p\text{H}_2 < 10.0$, the {100} family planes contribution just disappears and at that condition the morphology of the RuS2 particles is mainly determined by the (111) and (102) planes.

To explore the nature of the HDS active sites of the exposed surface, we have determined the atomic basins of their outermost
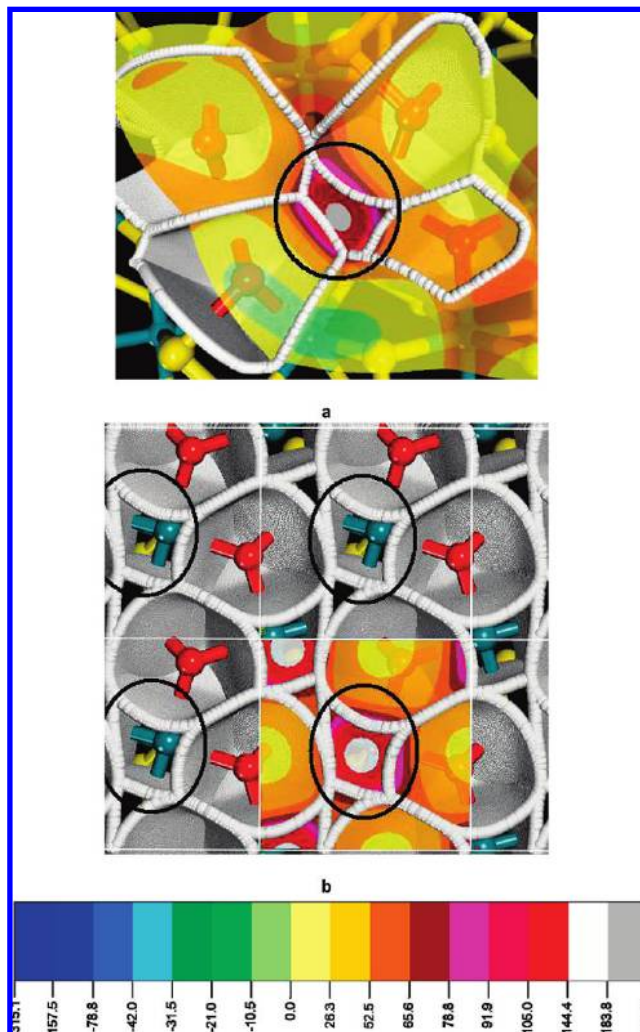

Figure 8. Electrostatic potential $V(\mathbf{r})$ color mapped on the cap of the outermost atomic basins for (a) 6S_111 and (b) 2S_100 surfaces, respectively. The tab at the bottom is blue jay (−157.530 to −78.765 kJ/mol), blue heaven (−78.765 to 42.008 kJ/mol), light blue (−42.008 to −31.506 kJ/mol), dark green (−31.506 to −21.004 kJ/mol), green (−21.004 to −10.502 kJ/mol), light green (−10.502 to 0.000 kJ/mol), light yellow (0.000 to 26.255 kJ/mol), yellow cream (26.255 to 52.510 kJ/mol), orange (52.510 to 65.638 kJ/mol), brown (65.638 to 78.765 kJ/mol), purple (78.765 to 91.893 kJ/mol), light red (91.893 to 105.020 kJ/mol), red (105.020 to 144.403 kJ/mol), white (144.403 to 183.75 kJ/mol), and gray (185.75 to 236.295 kJ/mol). Black circles highlight the holes defining the most acid sites.

individual atoms, i.e., the volume spanned by the $\rho(\mathbf{r})$ gradient paths ending at a given nucleus.[32] Direct visualization of the basin of the outermost atoms allows us to locate the most accessible Lewis acid site (the CUS) to the exterior of the surfaces.[18,67] Figure 7a shows a top view of the optimized 6S_111 surface. This surface exposes 5-coordinated Ru atoms (dark blue spheres), surrounded by four outermost S atoms (red spheres). Small gray spheres denote the Ru−S bond critical points defining the interatomic border of the atomic basin. The basins (white walls) for just the four exposed S atoms surrounding each outermost Ru are shown in Figure 7b. We can see that a hole just at the middle of the sulfur basins provides access to uncovered metal sites. Theses zones should be the stronger Lewis acid sites at the surface. Similar atomic basin visualizations of the outermost sulfur atoms of MoS2 edges[18] and Ni3S2 surfaces[68] have shown that these sulfur atoms tend to cover and encapsulate the outermost metallic atoms, while

Low Miller Index RuS$_2$ Surfaces

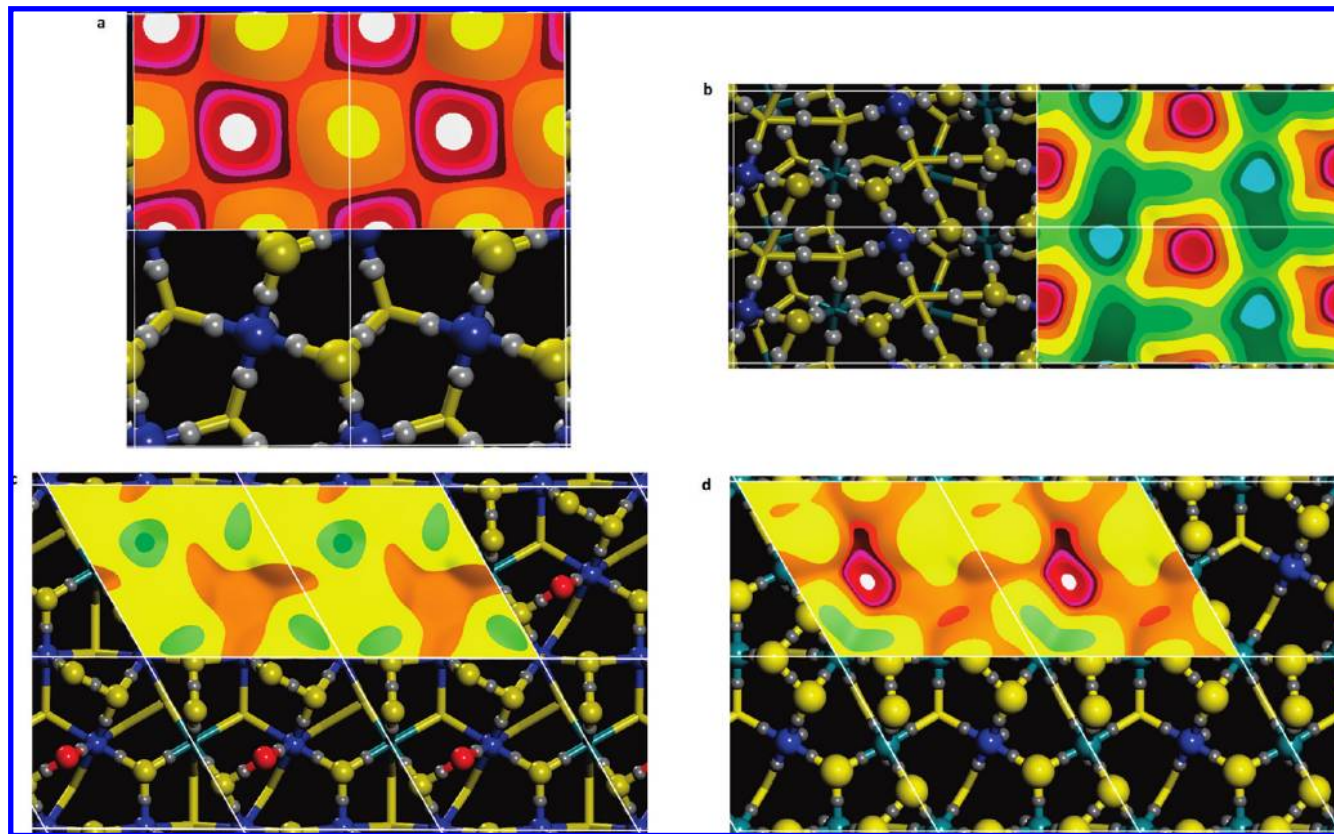*J. Phys. Chem. C, Vol. 113, No. 45, 2009* **19555**

Figure 9. Top-view of the $V(\mathbf{r})$ values color mapped onto the 0.001 au $\rho(\mathbf{r})$ isocontour for (a) 2S_100, (b) 5S_102, (c) 7S_111 and (d) 6S_111 RuS$_2$ surfaces, respectively. The color scale is the same as in Figure 8. Yellow and dark blue spheres denote the outermost S and Ru atoms, respectively.

for NiMoS edges;[67] holes between the sulfur basins correspond to the site where the Ni and Mo atoms are most accessible to the incoming molecules.

Exposed surface atoms, such as an atom in an isolated molecule, have considerable open parts that extend to infinity. These atoms are open or unbounded at the exterior of the surface, and a practical definition[18,32,40,67] is to cap the atom with an isosurface of the electron density with small $\rho(\mathbf{r})$ value representing the van der Waals envelope of the system. This isosurface (usually $\rho(\mathbf{r}) = 0.001$ au) can be considered as the practical outer limit of the atoms in molecules, crystals, or surfaces because, in general, it encompasses at least 95% of the electronic charge of the system.[87] Figure 7c shows such an isosurface superposed on the atomic basins of one of the sulfur atoms illustrated in Figure 7b. We can see clearly as the $\rho(\mathbf{r}) = 0.001$ isosurface defines the edge (outer limit) of one of the outermost S atoms.

HDS susceptibility of the sites on the exposed atoms can be particularly explored by mapping the electrostatic potential on the $\rho(\mathbf{r})$ isosurface capping them.[18,67] Such a mapping allows us to identify the host sites in which nucleophiles (most positive zone) and electrophiles (most negative zone) should bind. Additionally, the local maximum value of $V(\mathbf{r})$ at the determined host zones provides a quantitative determination of the Lewis acidity strength on the outermost atoms. A top view of the $V(\mathbf{r})$ color maps for the (6S_111) and (2S_100) surfaces are shown in Figure 8. Starting from the most negative $V(\mathbf{r})$ values (see the caption of Figure 8), three different tones of blue and three of green are used to represent the range of most negative $V(\mathbf{r})$ values while two yellow tones, one orange, one brown, one purple, two red tones, one white and one gray, respectively, denote the positive $V(\mathbf{r})$ values. The color map exhibits small

areas of strong Lewis acid white zones localized at the centers of each four outermost Ru atoms, just at small holes between the basins of the outermost S atoms (See Figures 8a and 8b). These white regions correspond to sites of highly positive $V(\mathbf{r})$ values, and therefore to the most Lewis acidic sites.

Figure 9 shows details of the $V(\mathbf{r})$ color maps for the 2S_100, 5S_102, 7S_111, and 6S_111 surfaces. According to our morphology study, these are the surface phases that might be exposed in isolated RuS$_2$ nanoparticles. These maps exhibit white zones above each outermost five-coordinated Ru atoms (dark blue spheres) for 2S_100 (Figure 9a) and 6S_111 (Figure 9d) surfaces, respectively, with a local maximum of 181.16 and 160.16 kJ/mol, respectively, and red zones above similar coordinated Ru atoms with a local maximum of 139.16 kJ/mol for the 5S_102 one (Figure 9b). These findings suggest that the above surfaces are much stronger Lewis acids than the exposed (111) and (11−1) surfaces, in Ni$_3$S$_2$ nanoparticles[68] with Vmax= 52.51 and 36.76 kJ/mol, respectively, and than NiMoS edges[67] models with 100% (Vmax=81.39 kJ/mol), 33% (Vmax=79.82 kJ/mol) and 66% (66.69 kJ/mol) of Mo atoms substituted by Ni atoms. Additionally, the present RuS$_2$ surfaces would show a similar Lewis acidity as compared to the acidity of Mo-sites on the NiMoS edge ($V_{max} = 210.30$ kJ/mol), at which just one outermost S atom has been removed.[67]

For the 7S_111 surface, the most positive zones (Figure 9c) correspond to light yellow regions localized above the outermost metal atoms and contain a local maximum of 47.26 kJ/mol. These results show that the 7S_111 termination exposes much weaker Lewis acids than the other surfaces. In fact, its Lewis acidity should be smaller compared to that of Ni$_3$S$_2$ exposed surfaces (52.51 kJ/mol),[68] one of the less active HDS catalysts. In agreement with our morphology results, this 7S_111 surface

should be present at low temperature and high reduction conditions. HDS conditions become a destabilizing factor for the 7S_111 termination and lead preferentiality to the 2S_100, 5S_102, and 6S_111 surfaces. At these reaction conditions, around 80% of the RuS$_2$ particles will expose 2S_100 and 6S_111 surfaces and therefore a high concentration of strong Lewis acid sites. These findings contrast with those in the Ni$_3$S$_2$ particles case, whose surface area is completely (100%) covered with very week Lewis acid sites.[68] At the same conditions, the determined RuS$_2$ Lewis acidity is quite similar to the corresponding acidity of the most acid site on the NiMoS particles ($V_{max} = 210.30$ kJ/mol). However, similar thermodynamics and morphology studies[93] have suggested that less than 10% of the exposed area of the NiMoS particles is covered with this kind of sites.

In summary, the present results suggests that the origin of the high HDS reactivity of RuS$_2$ catalysts is strongly related to the high concentration of strong Lewis acid sites at the surfaces exposed by catalyst particles. More factors such as support and particle size effects, hydrogen adsorbed in the form of S−H and M-H groups, steric effect of the Lewis basic sites (outermost S toms) covering the metal sites impeding its interaction with the incoming molecules, etc., must be considered. We are currently exploring such factors in our laboratory.

4. Conclusions

First-principles surface thermodynamics and morphologic studies suggest that nonsupported RuS$_2$ nanoparticles would expose just 2S_100, 6S_111, and 5S_102 surface phases in HDS conditions of temperature and ratio of the gas-mixture partial pressures. A very high Lewis acidity at these surface sites is suggested by the nature of the electrostatic potential projected at the electronic density contour corresponding to a $\rho(\mathbf{r})$ value of 0.001 au. Consequently, the S atoms contained in the polluting molecules are very attracted by the surface sites exposed by RuS$_2$ surface cuts. These results suggest that the origin of the observed high HDS reactivity of RuS$_2$ catalysts is strongly related to the high concentration of strong Lewis acid sites at the surfaces exposed by the catalyst particles.

References and Notes

(1) (a) Weisser, O.; Landa, S. *Sulfide Catalysts: Their Properties and Applications*; Pergamon: Oxford, 1973. (b) Hinnemann, B.; Moses, P. G.; Norskov, J. K. *J. Phys.: Condens. Matter* **2008**, *20*, 064236.

(2) Topsoe, H.; Clausen, B. S.; Massoth, F. *Hydrotreating Catalysis in Catalysis, Science and Technology*; Springer Verlag: Berlin, 1996; Vol. 11.

(3) Rodriguez, J. A.; Drovak, J.; Capitano, A. T.; Gabelnick, A. M.; Gland, J. L. *Surf. Sci.* **1999**, *429*, L462.

(4) Pecoraro, T. A.; Chianelli, R. R. *J. Catal.* **1981**, *67*, 430.

(5) Chianelli, R. R.; Daage, M.; Ledoux, M. J. *Adv. Catal.* **1994**, *40*, 117.

(6) Harris, S.; Chianelli, R. R. *J. Catal.* **1984**, *86*, 400.

(7) Chianelli, R. R.; Berhault, G.; Raybaud, P.; Kasztelan, S.; Hafner, J.; Toulhoat, H. *Appl. Cat. A: General* **2002**, *227*, 83.

(8) Chianelli, R. R.; Daage, M.; Ledoux, M. J. *Adv. Catal.* **1994**, *40*, 117.

(9) Toulhoat, H.; Raybaud, P. *J. Catal.* **2003**, *216*, 63.

(10) Vissers, J. P. R.; Groot, C. K.; Vanoers, E. M.; de Beer, V. H. J. *Bull. Soc. Chim. Belg.* **1984**, *93*, 813.

(11) Ledoux, M. J.; Michaux, O.; Agostini, G.; Panisso, P. *J. Catal.* **1986**, *102*, 275.

(12) Burdett, J. K.; Chung, J. T. *Surf. Sci. Lett.* **1990**, *236*, L353.

(13) Smith, T. S.; Johnson, K. H. *Catal. Lett.* **1994**, *28*, 361.

(14) Raybaud, P.; Kresse, G.; Hafner, J.; Toulhoat, H. *J. Phys.: Condens. Matter.* **1997**, *9*, 11085.

(15) Raybaud, P.; Hafner, J.; Kresse, G.; Kasztelan, S.; Toulhoat, H. *J. Catal.* **2000**, *190*, 128.

(16) Neurock, M.; van Santen, R. A. *J. Am. Chem. Soc.* **1994**, *116*, 4427.

(17) Aray, Y.; Rodríguez, J.; Vega, D.; Rodriguez-Arias, E. N. *Angew. Chem. Int. Ed.* **2000**, *39*, 3810.

(18) Aray, Y.; Rodríguez, J. *J. Mol. Catal. A: Chem.* **2007**, *265*, 32.

(19) Raybaud, P.; Hafner, J.; Kresse, G.; SKasztelan, S.; Toulhoat, H. *J. Catal.* **2000**, *189*, 129.

(20) Clausen, B. S.; Lengeler, B.; Candia, R.; Als-Nielsen, J.; Topsoe, H. *Bull. Soc. Chim. Belg.* **1981**, *90*, 1249.

(21) Parham, T. G.; Merrill, R. P. *J. Catal.* **1984**, *85*, 295.

(22) Tauster, S. J.; Pecoraro, T. A.; Chianelli, R. R. *J. Catal.* **1980**, *63*, 515.

(23) Topsoe, H.; Candia, R.; Topsoe, N. Y.; Clausen, B. S. *Bull. Soc. Chim. Belg.* **1984**, *93*, 783.

(24) (a) Lauritsen, J. V.; Bollinger, M. V.; Lægsgaard, E.; Jacobsen, K. W.; Nørskov, J. K.; Clausen, B. S.; Topsøe, H.; Besenbacher, F. *J. Catal.* **2004**, *221*, 510. (b) Schweiger, H.; Raybaud, P.; Toulhoat, H. *J. Catal.* **2002**, *212*, 33. (c) Schweiger, H.; Raybaud, P.; Kresse, G.; Toulhoat, H. *J. Catal.* **2002**, *207*, 76.

(25) Rodríguez, J. A.; Tanhong, C.; Zhen, S.; Hrbek, J. *J. Am. Chem. Soc.* **2004**, *126*, 8886.

(26) (a) Grillo, M. E.; Smelyanski, V.; Sautet, P.; Hafner, J. *Surf. Sci.* **1999**, *439*, 163. (b) Grillo, M. E.; Sautet, P. *Surf. Sci.* **2000**, *457*, 285. (c) Grillo, M. E.; Sautet, P. *J. Mol. Catal. A: Chem.* **2001**, *174*, 239.

(27) Aray, Y.; Rodríguez, J.; Vega, D.; Coll, S.; Rodríguez-Arias, E. N.; Rosillo, F. *J. Phys. Chem. B* **2002**, *106*, 13242.

(28) (a) Padilla, J.; Vanderbilt, D. *Phys. Rev. B* **1997**, *56*, 1625. (b) Wang, X.-G.; Weiss, W.; Shaikhutdinov, Sh. K.; Ritter, M.; Petersen, M.; Wagner, F.; Schlögl, R.; Scheffler, M. *Phys. Rev. Lett.* **1998**, *81*, 1038. (c) Finnis, M. W. *Phys. Stat. Sol. A* **1998**, *166*, 397. (d) Grillo, M. E.; Ranke, W.; Finnis, M. W. *Phys. Rev. B* **2008**, *77*, 075407. (e) Rogal, J.; Reuter, K.; Scheffler, M. *Phys. Rev. B* **2004**, *69*, 075421. (f) Li, W.-X.; Stampfl, C.; Scheffler, M. *Phys. Rev. B* **2003**, *68*, 165412. (g) Reuter, K.; Scheffler, M. *Phys. Rev. B* **2001**, *65*, 035406. (h) Soon, A.; Todorova, M.; Delley, B.; Stampfl, C. *Phys. Rev. B* **2007**, *75*, 125420. (i) Raybaud, P.; Costa, D.; Corral-Valero, M.; Arrouvel, C.; Digne, M.; Sautet, P.; Toulhoat, H. *J. Phys.: Condens. Matter* **2008**, *20*, 064235.

(29) Krebs, E.; Silvi, B.; Raybaud, P. *Catal. Today* **2008**, *130*, 160.

(30) Costa, D.; Arrouvel, C.; Breysse, M.; Toulhoat, H.; Raybaud, P. *J. Catal.* **2007**, *246*, 325.

(31) Arrouvel, C.; Breysse, M.; Toulhoat, H.; Raybaud, P. *J. Catal.* **2005**, *232*, 161.

(32) (a) Bader, R. F. W. *Atoms in molecules-a quantum theory*; Clarendon Press: Oxford, U.K., 1990. (b) Bader, R. F. W. *Chem. Rev.* **1991**, *91*, 893.

(33) Bader, R. F. W. *J. Phys. Chem. A* **1998**, *102*, 7314.

(34) Bader, R. F. W.; Popelier, P. L. A.; Keith, T. A. *Angew. Chem. Int. Ed., Engl.* **1994**, *33*, 620.

(35) Zou, P. F.; Bader, R. F. W. *Acta Crystallogr.* **1994**, *A50*, 714.

(36) Eberhart, M. E. *J. Can. Chem. Soc.* **1996**, *74*, 1229.

(37) Eberhart, M. E. *Philos. Mag. A* **1996**, *73*, 47.

(38) Aray, Y.; Rodríguez, J.; Vega, D. *J. Phys. Chem. B* **2000**, *104*, 4608.

(39) Pendás, M. A.; Costales, A.; Luaña, V. *Phys. Rev. B* **1997**, *55*, 4275.

(40) Popelier, P. *Atoms in Molecules -An Introduction*; Prentice Hall: Harlow-England, 2000.

(41) Gillespie, R. J.; Popelier, P. L. A. *Chemical Bonding and Molecular Geometry: From Lewis to Electrón Densities*; Oxford University Press: New York, 2001.

(42) Ghermani, N. E.; Lecomte, C.; Dusausoy, Y. *Phys. Rev. B* **1996**, *53*, 4231.

(43) Hénaff, C. L.; Hansen, N. K.; Protas, J.; Marnier, G. *Acta Crystallogr., B* **1997**, *53*, 870.

(44) Ivanov, Y. V.; Belokoneva, E. L.; Protas, J.; Hansen, N. K.; Tirelson, V. G. *Acta Crystallogr. B* **1998**, *54*, 774.

(45) Koritsanszky, T. S.; Coppens, P. *Chem. Rev.* **2001**, *101*, 1583.

(46) Downs, R. T.; Gibbs, G. V.; Boisen, M. B., Jr.; Rosso, K. M. *Phys. Chem. Miner.* **2002**, *29*, 369.

(47) Abramos, Y. A.; Okamura, F. P. *Acta Crystallogr. A* **1997**, *53*, 187.

(48) Takata, M.; Sakata, M.; Kumazawa, S.; Larsen, F. K.; Iversen, B. *Acta Crystallogr. A* **1994**, *50*, 330.

(49) Vyboishchikov, S. F.; Masunov, A. E.; Streltsov, V. A.; Zorkii, P. M.; Tirelson, V. G. *Zh. Fiz. Khim.* **1994**, *68*, 2024.

(50) Boese, R.; Boese, A. D.; Blazer, D.; Antipin, M. Y.; Ellern, A.; Seppelt, K. *Angew. Chem., Int. Ed. Engl.* **1997**, *36*, 1489.

(51) Boese, R.; Niederprum, N.; Blazer, D.; Maulitz, A.; Antipin, M. Y.; Mallison, P. R. *J. Phys. Chem. B* **1997**, *101*, 5794.

(52) Munshi, P.; Guru Row, T. N. *Crystallogr. Rev.* **2006**, *11*, 199.

Low Miller Index RuS$_2$ Surfaces

J. Phys. Chem. C, Vol. 113, No. 45, 2009 **19557**

(53) Mei, C. J.; Edgecombe, K. E.; Smith, V. H.; Heilingbrunner, A. *Int. J. Quantum Chem.* **1993**, *48*, 287.

(54) Aray, Y.; Rodríguez, J.; Rivero, J. *J. Phys. Chem. A* **1997**, *101*, 6976.

(55) Mori-Sánchez, P., *Densidad electrónica y enlace químico. De la molécula al cristal*. Ph.D. Thesis, Universidad de Oviedo, 2002.

(56) Eberhart, M. E.; Clougherty, D. P.; MacLaren, J. M. *J. Am. Chem. Soc.* **1993**, *115*, 5762.

(57) Eberhart, M. E.; Clougherty, D. P.; MacLaren, J. M. *J. Mater. Res.* **1993**, *8*, 438.

(58) Haussermann, U.; Wengert, S.; Nesper, R. *Angew. Chem., Int. Ed. Engl.* **1994**, *33*, 2073.

(59) Grosch, G. H.; Range, K. J. *J. Alloys Compd.* **1996**, *233*, 39.

(60) Knecht, M.; Ebert, H.; Bensch, W. *J. Alloys Compd.* **1997**, *246*, 166.

(61) Tirelson, V. G.; Zou, P. F.; Tang, T. H.; Bader, R. F. W. *Acta Crystallogr. A* **1995**, *51*, 143.

(62) Gatti, C.; Saunders, V. R.; Roetti, C. *J. Chem. Phys.* **1994**, *101*, 10686.

(63) Plats, J. A.; Howard, S. T. *J. Chem. Phys.* **1996**, *105*, 4668.

(64) Luaña, V.; Costales, A.; Mori-Sánchez, P.; Pendás, M. A. *J. Phys. Chem. B* **2003**, *107*, 4912.

(65) Blanco, M. A.; Costales, A.; Pendás, A. M.; Luaña, V. *Phys. Rev. B* **2000**, *62*, 12028.

(66) Pendás, A. M.; Costales, A.; Luaña, V. *Phys. Rev. B* **1997**, *55*, 4285.

(67) Aray, Y.; Rodríguez, J.; Vidal, A. B.; Coll, S. *J. Mol. Catal. A: Chem.* **2007**, *271*, 105.

(68) Aray, Y.; Vega, D.; Rodríguez, J.; Vidal, A. B.; Grillo, M. E.; Coll, S. *J. Phys. Chem. B* **2009**, *113*, 3058.

(69) Reuter, K.; Stampfl, C.; Scheffler, M. *Handbook of Materials Modeling-Ab initio Thermodynamics and Statistical Mechanics of Surface Properties and Functions*; Springer: Berlin, 2005, Vol 1.

(70) Cristol, S.; Paul, J. F.; Payen, E.; Bougeard, D.; Clemendot, S.; Hutschka, F. *J. Phys. Chem. B* **2000**, *104*, 11220.

(71) Raybaud, P. *Appl. Catal. A: General* **2007**, *322*, 76.

(72) DMol³ is available as part of Material Studio. Accelrys Inc.: San Diego, CA, 2002.

(73) Delley, B. *J. Chem. Phys.* **1990**, *92*, 508; **2000**, *113*, 7756.

(74) Leboeuf, M.; Koster, M.; Jug, K.; Salahub, D. R. *J. Chem. Phys.* **1999**, *111*, 4893.

(75) Gadre, S. R.; Shirsat, R. N. *Electrostatics of Atoms and molecules*; Universities Press: Hyderabad, 2000.

(76) (a) Pingale, S. S.; Gadre, S. R.; Batolotti, L. J. *J. Phys. Chem. A* **1998**, *102*, 9987. (b) Deshmukh, M. M.; Sastry, N. V.; Gadre, S. R. *J. Chem. Phys.* **2004**, *121*, 12402. (c) Joshi, K. A.; Gejji, S. P. *J. Mol. Struc. THEOCHEM* **2005**, *724*, 87. (d) Tachikawa, H.; Iyama, T.; Kawabata, H. *J. Mol. Struc. THEOCHEM* **2005**, *718*, 117.

(77) (a) Pathak, R. K.; Gadre, S. R. *J. Chem. Phys.* **1990**, *93*, 1770. (b) Gadre, S. R.; Kulkarni, S. A.; Shrivastava, I. H. *J. Chem. Phys.* **1992**, *96*, 5253.

(78) Gadre, S. R.; Pathak, R. K. *Proc. Ind. Acad. Sci. (Chem. Sci)*. **1989**, *102*, 18.

(79) (a) Alhambra, C.; Luque, F. J.; Orozco, M. *J. Phys. Chem.* **1995**, *99*, 3084. (b) Kornelak, P.; Michalak, A.; Najbar, M. *Catal. Today.* **2005**, *101*, 175. (c) Michalak, A. *Chem. Phys. Lett.* **2004**, *386*, 346.

(80) Politzer, P.; Truhlar, D. G. *Chemical Applications of Atomic and Molecular Electrostatic Potentials*; Plenum: New York, 1982.

(81) Murray, J. S.; Sen, K. D. *Molecular Electrostatic Potential: Concepts and Applications*; Elsevier: Amsterdam, 1996.

(82) Orozco, M.; Luque, F. J. *Theoret. Comput. Chem. Ser.* **1996**, *3*, 181.

(83) Aray, Y.; Marquez, M.; Rodríguez, J.; Coll, S.; Simón-Manso, Y.; Gonzalez, C.; Weitz, D. A. *J. Phys. Chem. B* **2003**, *107*, 8946.

(84) (a) Aray, Y.; Marquez, M.; Rodríguez, J.; Coll, S.; Simón-Manso, Y.; Gonzalez, C.; Weitz, D. A. *J. Phys. Chem. B* **2004**, *108*, 2418. (b) Aray, Y.; Rodríguez, J.; Coll, S.; Gonzalez, C.; Marquez, M. *J. Phys. Chem. B* **2004**, *108*, 18942.

(85) Tal, Y.; Bader, R. F. W.; Erkku, J. *Phys. Rev. A* **1980**, *21*, 1.

(86) Keith, T. A.; Bader, R. F. W.; Aray, Y. *Int. J. Quantum Chem.* **1996**, *57*, 183.

(87) (a) Parr, R. G.; Lee, C. *J. Chem. Phys.* **1991**, *94*, 6055. (b) Sjoberg, P.; Politzer, P. *J. Phys. Chem.* **1990**, *94*, 3959. (c) Sjoberg, P.; Politzer, P. *J. Chem. Phys.* **1983**, *79*, 3859.

(88) Aray, Y.; Rodriguez, J.; Vega, D. In *The Quatum Theory of Atoms in Molecules: From DNA to Solid and Drug Design*; Matta, C. F., Boyd, R. J., Eds.; Wiley-VCH: Weinheim, 2006.

(89) Aray, Y.; Rodríguez, J.; Coll, S.; Rodríguez-Arias, E.; Vega, D. *J. Phys. Chem. B* **2005**, *109*, 23564.

(90) Perdew, J. P.; Burke, K.; Emzerhof, M. *Phys. Rev. Lett.* **1996**, *77*, 3865.

(91) Lutz, H. D.; Mueller, B.; Schmidt, T.; Sting, T. *Acta Crystallogr. C* **1990**, *46*, 2003.

(92) Aouine, M.; Geantet, C.; Epicier, T. *Catal. Today* **2001**, *66*, 91.

(93) Guernalec, N.; Geantet, P.; Raybaud, P.; Cseri, T.; Aouine, M.; Vrinat, M. *Oil Gas Sci. Technol.-Rev. IFP* **2006**, *61*, 515.

(94) Diaz, D.; Castillo-Blum, S. E.; Alvarez-Fregoso, O.; Rodriguez-Gattorno, G.; Santiago-Jacinto, P.; Rendon, L.; Ortiz-Frade, L.; Leon-Paredes, Y.-J. *J. Phys. Chem. B* **2005**, *109*, 22715.

(95) Wulff, G. *Z. Kristallogr.* **1901**, *34*, 449.

(96) (a) Mittendorfer, F.; Seriani, N.; Dubay, O.; Kresse, G. *Phys. Rev. B* **2007**, *76*, 233413. (b) Baetzold, R. C.; Yang, H. *J. Phys. Chem. B* **2003**, *107*, 14357. (c) Wang, L.; Zhou, F.; Meng, Y. S.; Ceder, G. *Phys. Rev. B* **2007**, *76*, 165435. (d) Zhu, W.; Jin, H. M.; Wu, P.; Liu, H. L. *Phys. Rev. B* **2004**, *70*, 165419.

(97) KrystalSaper is available as part of JcrystalSoft 2005−2009; www.jcrystal.com.

JP809020T